# Feature-Enhancing Inverse Methods for Limited-View Tomographic Imaging Problems

Eric Miller[1], Margaret Cheney[2], Misha Kilmer[3], Gregory Boverman[1], Ang Li[4,5], David Boas[4]

[1] Center for Subsurface Sensing and Imaging Systems,
Dept. of Electrical and Computer Engineering, 302 Stearns Center,
Northeastern University, Boston MA, 02115, {elmiller,gboverma}@ece.neu.edu

[2]Department of Mathematical Sciences, Amos Eaton Hall,
Rensselaer Polytechnic Institute,
110 Eighth Street, Troy, NY 12180, cheney@rpi.edu

[3]Dept. of Mathematics, 113 Bromfield-Pearson Bldg.
Tufts University, Medford, MA 02155, mkilme01@tufts.edu

[4] Athinoula A. Martinos Center for Biomedical Imaging
Massachusetts General Hospital, Harvard Medical School, Charlestown, MA 02129

[5] Electrical Engineering Department, Tufts University, Medford MA 02115.

May 21, 2003

**Abstract**

In this paper we overview current efforts in the development of inverse methods which directly extract target-relevant features from a limited data set. Such tomographic imaging problems arise in a wide range of fields making use of a number of different sensing modalities. Drawing these problem areas together is the similarity in the underlying physics governing the relationship between that which is sought and the data collected by the sensors. After presenting this physical model, we explore its use in two classes of feature-based inverse methods. Microlocal techniques are shown to provide a natural mathematical framework for processing synthetic aperture radar data in a manner that recovers the edges in the resulting image. For problems of diffusive imaging, we describe our recent efforts in parametric, shape-based techniques for directly estimating the geometric structure of an anomalous region located against a perhaps partially-known background.

# 1 Introduction

According to its Greek entomology, the word *tomography* refers to the synthesis of an image covering a single slice (*tomos*) of a medium [55]. Over the past few decades however this term has come to encompass a much broader range of information-extraction procedures operating at the single-slice as well as volumetric level. In this paper we consider tomography to encompass any processing method in which one seeks to obtain information concerning the spatial variations of the physical parameters of a medium from observations of scattered energy or radiation collected at or near the boundary. In particular, we concentrate on *limited view* tomographic problems in which the information content of data is in some way restricted, thereby complicating the problem of robustly constructing an image. In many cases, the limitations are spatial in that the transmitting and receiving sensors are restricted from fully encircling region of interest. In other cases, the limitations are induced by the physics of the problem which filter the information in the data pertaining to the distribution of the underlying parameters. Many applications suffer from both of these difficulties. In this paper we provide an overview of recent work in our group on a number of "feature-based" inversion approaches which can be widely employed across a range of limited view problems.

As background, in Table 1 we indicate a few of the many problem areas, processing objectives, and representative sensing modalities characteristic of this class of imaging problems. While the specifics of the problems are quite variable, there are a number of common underlying themes which imply that models and algorithms developed in one domain may be applicable in other areas as well. One readily apparent level of commonality is provided in terms of the sensing modalities. Low frequency electromagnetic sensors are used in a variety of geophysical as well as military applications [25, 54, 62, 63]. Similarly, acoustic and radar sensing play a key role in many non-destructive evaluation (NDE), military, and biomedical imaging problem areas [1,12,14,15,21,48]. At a slightly more abstract level, even when the sensors differ, the underlying physics can be remarkably similar. As an example, photothermal methods for NDE, diffuse-optical techniques for medical imaging, and (in a limiting sense) electrical-resistance/impedance sensing in geophysics and medicine all can be described within the context of a scalar Helmholtz equation or its limiting case of Poisson's equation [16, 41, 43, 44, 47, 65]. Thus, tools developed in one regime should in principle be portable

to others. Finally, even when the sensors and physics differ, the underlying processing objective can be quite similar. For many problems, the goal is not so much a detailed image of the full medium, but rather, the detection and characterization of anomalous regions (e.g. tumors, material flaws, buried landmines, or pollution plumes) in a perhaps unknown or partially-known background. For cases such as these, one would expect that general-purpose techniques for parameterizing these anomalies and background along with the algorithms for estimating these parameters from data should again be able to function across a wide range of application areas and sensing modalities.

The common structure in these limited view problems has led to a relatively well defined set of processing schemes having wide applicability. One the one hand, there has been significant development in pixel-based reconstruction strategies. Indeed, for problems employing X-ray radiation or where the object represents a small perturbation about the background, well known, analytical methods such as filtered backprojection [33] or diffraction tomography [26, 28] have proven remarkably successful in producing high-quality images. Even when the assumptions underlying these methods are violated, variants of these schemes still are employed with success.

In contrast to these analytical methods, a fundamentally different approach taken for the limited view imaging problem is based on the use of variational principles in which the estimate of the pixels in the image (or voxels in the volume) are defined as the solution to an optimization problem [3, 9, 27, 40, 47, 61, 64]. The optimizing functional is comprised of one term which requires that the recovered image, when passed through a computational model of the sensor physics, yields a "good" fit to the data. Other terms are also appended in order to encourage the reconstructed image to have certain *a priori* specified characteristics. These *regularizers* mathematically stabilize the results of the optimization procedure and are required to overcome the inherent lack of information in the data caused by the limited view nature of the problem. Most often these characteristics are related to some measure of the smoothness of recovered image [4, 60].

While this image-based approach to limited view tomography is quite flexible and has proven to be quite effective, here we consider approaches to this class of problems which are less tuned toward pixel recovery and more aimed at extracting directly from the data information regarding "features" of the unknown scene directly linked to the underlying processing objective (characterization of

buried objects, tumor localization, etc.). Thus, we are particularly concerned with those limited view problems that are of the anomaly detection and characterization variety.

In this field alone there has been significant work in a number of communities over the past ten to twenty years. In the applied mathematics and mathematical physics communities, inverse obstacle problems have been widely studied by a number of groups. As in the imaging case, more analytically-oriented schemes known as dual-space [23], level-set [29, 42], and linear sampling techniques [13, 22, 24, 32, 58] have long and very interesting histories. Variational approaches to shape reconstruction have also been a source of much work [19, 20, 35, 39, 46]. In the signal and image processing communities, statistical techniques for estimating the structure of ellipses and understanding bounds on performance under assumed models for data noise given X-ray type data have been considered in [57]. Extension of these methods to ellipsoids was the subject of work in [34]. As a final example, the ability to determine the structure of binary polygonal objects was considered in [45].

The goal of this paper is to describe some recent work being pursued in our group in this area of geometric feature-based inversion for limited view tomography problems. Specifically we concentrate on two very different methods. On the analytical side, microlocal techniques are considered for problems in airborne synthetic aperture radar (SAR) imaging. With roots in the mathematical geophysics community [5], these methods exploit some very deep structure of the underlying physics to stably producing imagery in which edge-like features are highlighted. In the SAR context, these edges represent features characteristic of objects on the ground which may be of military significance such as tanks, trucks, or artillery.

In terms of variational techniques, an overview of our efforts in the application of parametric shape based schemes is provided. Following the work in [35, 46], this approach reduces inversion to a parameter estimation problem where the quantities to be determined describe the geometric structure of the anomaly. Unlike this previous work, we apply our methods to a highly non-linear tomographic imaging problem arising in diffuse optical tomography (DOT) [2, 7, 52, 53]. Here, the move away from X-ray type of problems has lead to the synthesis of new methods for solving the resulting optimization problem.

While the exposition in this paper is limited to the use of SAR for illustrating the microlocal work and DOT for the shape-based schemes, we emphasize that our feature-based approaches have much wider applicability than these two areas. In addition to its utility in geophysical applications, the microlocal tomography holds promise for use in any area where sharp edges separate the object of interest from the nominal background e.g. NDE, landmine detection, or buried facility imaging. Similarly, the fact that our shape-based methods describe a way of parameterizing the unknown, imply applicability in a range of areas again like landmines, but also geophysical exploration and the like.

The remainder of this paper is organized as follows. In § 2 a common physical model sufficiently rich to encompass both the SAR application as well as DOT is presented. Using this model, the microlocal techniques are described in § 3 while the geometric methods are the subject of § 4. Finally § 5 is devoted to conclusions and an indication as to directions for future work.

## 2 Physical Model

The physical model underlying all of the applications of interest in this paper as well as a number of others considered by our group and others takes the form of a scalar, frequency domain type of Helmholtz equation or its time domain, wave-equation counterpart. We begin in the frequency domain with

$$\nabla \cdot \sigma(r) \nabla \phi(r) + k^2(r, \omega)\phi(r) = s(r) \tag{1}$$

plus boundary conditions with $s(r)$ the source and $\omega$ the modulation frequency. In (1), $\phi$ represents the electromagnetic, acoustic, or diffusive field. Measurements of this field then provide the data for estimating the physical parameters of the medium which are related to the mathematical coefficients, $\sigma$ and $k^2$. For DOT, in terms of the desired optical absorption and scattering parameters, $\mu_a(r)$ and $\mu_{s'}(r)$ respectively, we have $\sigma = 1/3\mu_s'$ and $k^2 = \sqrt{-1}\omega - c\mu_a$ with $c$ the speed of light in the medium [2]. For electrical resistance or electrical impedance tomography [16, 65] (another related class of frequency domain inverse problems), $k^2 = 0$, since we are probing at DC and $\sigma$, the electrical conductivity for resistance tomography or complex electrical permittivity for

impedance imaging, is the desired quantity. In the case of higher frequency electromagnetic inverse problems such as SAR, the physical quantities of interest are the electromagnetic permittivity, $\epsilon$, and conductivity, $\sigma$ [8]. For this class of problems, the quantity $\sigma$ in (1) is generally absorbed into $k^2$ which is a function of the physical parameters via:

$$k^2 = \omega^2 \mu_0 \left( \epsilon - \sqrt{-1} \frac{\sigma}{\omega} \right)$$

A number of popular inversion methods are also based on domain integral equation formulations of (1) [17,18,37]. These models assume that the image of interest represents a perturbation about a presumably known background. While such methods can be derived for reconstructing both $\sigma$ and $k^2$, for simplicity, here we consider only the later and moreover assume that $\sigma(r) = \sigma_0$, a constant. To derive these integral equations, we start by writing $k^2$ as

$$k^2(r) = k_b^2(r) + k_p^2(r) \tag{2}$$

with $k_b^2$ the known (possibly space varying) background and $k_p^2$ the unknown perturbation. Substitution of (2) into (1) and rearranging yields

$$\nabla \cdot \sigma_0 \nabla \phi(r) + k_b^2(r)\phi(r) = s(r) - k_p^2(r)\phi(r). \tag{3}$$

The key point here is that, if $k_b^2$ is suitably chosen, one can easily, and typically analytically, solve for the background "impulse response" of the medium. This quantity, also known as the Green's function and denoted $G(r, r')$, is the field generated at a point $r$ due to an impulsive source at location $r'$ [18, 38]. Formally, we have

$$\nabla \cdot \sigma_0 \nabla G(r, r') + k_b^2(r) G(r, r') = \delta(r - r'). \tag{4}$$

Given knowledge of $G$, by superposition, the field due to a spatially distributed source, say $\tilde{s}(r)$, is

$$\phi(r) = \int_{\mathbb{R}^3} G(r, r') \tilde{s}(r') dr'. \tag{5}$$

In the case where $k_b^2$ is constant, $G(r, r') = G(r - r')$ and (5) represents a multidimensional convolution. For more complex backgrounds such as layered media , the Green's function is not a spatially stationary and the convolutional nature of the integral is lost [18, Chapter 7].

To arrive at the final integral equation used for inverse problems, we let $\tilde{s} = s(r) - k_p^2(r)\phi(r)$ to obtain the second-kind integral equation for $\phi(r)$

$$\phi(r) = \int_{\mathbb{R}^3} G(r, r')s(r')dr' + \int_{\mathbb{R}^3} G(r, r')\phi(r')k_p^2(r')dr'. \tag{6}$$

The first term on the right hand side of (6), denoted as $\phi_b(r)$, is typically called the *background field* as it is the field which exists in the medium when $k_p^2 = 0$. In turn, the second term represents the *scattered* field in recognition of the fact that it is the contribution to $\phi$ due to interaction with (i.e. scattering from) the perturbation.

One of the key difficulties of inverse scattering problems in general as well as the limited view problems of interest here is the non-linearity in the relationship of the data to the material properties. Assuming that the data we measure are either the fields sampled at the surface of the medium or linear functionals of those field (e.g. the convolution of the fields with a sensor impulse response), the nonlinearity can be seen in two ways based on the developments in this section. Abstractly, we write (1), as $\mathcal{L}(\sigma, k^2)\phi = s$ with $\mathcal{L}$ representing the partial differential operator $\nabla \cdot \sigma\nabla + k_b^2(r)$ plus boundary conditions. Then we have $\phi = \mathcal{L}^{-1}(\sigma, k^2)s$ emphasizing that even though $\sigma$ and $k^2$ enter the PDE linearly, their relationship to the fields via the inverse of $\mathcal{L}$ is highly nonlinear. Alternatively, defining the integral operator $\mathcal{G}(k^2)$ via $[\mathcal{G}(k^2)]\phi = \int G(r, r')\phi(r')k_p^2(r')dr'$, (6) indicates that $\phi = (\mathcal{I} - \mathcal{G}(k^2))^{-1}\phi_b$. Hence again on the assumption that our data are linearly related to the field we have

$$\phi(r) = \phi_b(r) + \int_{\mathbb{R}^3} G(r, r') \left[(\mathcal{I} - \mathcal{G}(k_p^2))^{-1}\phi_b\right](r')k_p^2(r')dr'. \tag{7}$$

The presence of the $k_p^2$ in the brackets again represents the underlying non-linearity of the inverse problem.

In cases where the perturbation is "small" in size and amplitude, the determination of $k_p^2$ from the data is generally made easier by linearizing the physics about the background. Such a procedure

is known as the first Born approximation [18,33] and is most easily explained in terms of the integral equation form of the physics. For $k_p^2$ small [18], the field in the scatterer, that is $\phi(r')$ in the second term on the right hand side of (6), can be approximated as the field in the absence of the scatterer, i.e. $\phi_b(r')$. Making this substitution results in

$$\phi(r) = \phi_b(r) + \int_{\mathbb{R}^3} G(r, r')\phi_b(r')k^2(r')dr' \tag{8}$$

which represents a simple linear relationship [1] between the unknown $k^2$ and the data $\phi(r)$. We note here that even when the assumptions required for validity of the Born approximation are not fulfilled, the related Rytov approximation can often be employed with some success. As explained more fully in [33], the Rytov method also results in a linear mapping between data and unknown; although the "data" in this case are related to the complex logarithm of the ratio of $\phi$ to $\phi_b$.

We conclude this section by presenting a model for Synthetic Aperture Radar (SAR). It is in the context of SAR that we will discuss the microlocal analysis methods. Unlike the frequency-domain model we have been considering to this point, SAR is inherently a time-domain system. Thus, we are interested in a temporal form of the integral in (8). Obtaining such an expression is only a matter of an inverse Fourier transform. We denote by $\varphi$ the Fourier transform of $\phi$ and by $g$ the Fourier transform of $G$. More specifically, the time domain Green's function $g$ (defined to be the value of the field at time $t$ and location $r$ due to a source radiating at time $t'$ and position $r'$) is [10]

$$g(t, t', r, r') = \frac{\delta(t - t' - |r - r'|/c)}{4\pi|r - r'|}. \tag{9}$$

For SAR the quantity to be imaged, $k_p^2$, takes the form $k_p^2 = \omega^2 V(r)$ with $V$ an effective "reflectivity function". Substituting these relations into the integral on the right hand side of the (8) and recognizing that frequency-domain multiplication by $\omega^2$ is double differentiation in the time domain yields

$$d(r, t) \equiv \varphi(r) - \varphi_b(r) = \int_{\mathbb{R}^3} \frac{V(r')}{4\pi|r - r'|} \frac{d^2}{dt^2} \varphi_b(t - |r - r'|/c)dr'. \tag{10}$$

[1] Technically: affine relationship due to the $\phi_b$ term

We note that since (8) was obtained using the Born approximation, (10) also depends on the Born approximation.

SAR sensors generally operate in free space environments. Consequently the background field due to a transmitter at location $r_0$ takes the form

$$\varphi_b(r', t) = \int_{\mathbb{R}} \frac{e^{i\omega(t-|r'-r_0|/c)}}{4\pi|r'-r_0|} A_1(\omega, r', r_0) d\omega \tag{11}$$

where $A_1$ is a function of the frequency content of the pulse and the radiating characteristics of the antenna. Upon substituting (11) into (10) and assuming that the receiver is co-located with the transmitter, we obtain the final model

$$D(r, t) = \int_{\mathbb{R}\times\mathbb{R}^3} \frac{e^{i\omega(t-2|r-r'|/c)}}{(4\pi)^2|r-r'|^2} A(\omega, r, r') V(r') d\omega dr' \tag{12}$$

with $A = -\omega^2 A_1$.

To summarize: In this section we have presented a number of scattering-type models which are employed by our group to explore the use of feature-based inversion schemes across a range of applications. For problems in diffuse optical imaging, we draw most heavily on non-linear PDE and integral equation models summarized by equations (1) and (6). The goal of the DOT inverse problem is to use measured values of field $\phi$ to extract information concerning the optical properties as specified in $\sigma$ and $k^2$. In the case of synthetic aperture radar, our approach is specified within the context of the first Born approximation in equation (12). Here we use the scattered field data, $D$, to estimate the reflectivity function, $V$.

## 3 Microlocal Techniques

Microlocal analysis is a mathematical theory for analyzing singularities. This is of interest for feature extraction because the features of interest, such as boundaries between different materials and edges in images, can generally be described as singularities in the appropriate function. The term "microlocal" refers to the fact that singularities have both a location and a direction.

### 3.1 Wavefront sets

We characterize target features by means of $V$'s singular structure, which we describe in terms of its wavefront set.

Mathematically the singular structure of a function can be characterized by its *wavefront set*, which involves both the location $r$ and corresponding directions $\xi$ of singularities [30, 31, 59].

**Definition.** The point $(r_0, \xi_0)$ is *not* in the wavefront set $WF(f)$ of the function $f$ if there is a smooth cutoff function $\psi$ with $\psi(r_0) \neq 0$, for which the Fourier transform $\mathcal{F}(f\psi)(\lambda\xi)$ decays rapidly (i.e., faster than any polynomial in $1/\lambda$) as $\lambda \to \infty$, uniformly for $\xi$ in a neighborhood of $\xi_0$.

This definition says that to determine whether $(r_0, \xi_0)$ is in the wavefront set of $f$, one should 1) localize around $r_0$ by multiplying by a smooth function $\psi$ supported in the neighborhood of $r_0$, 2) Fourier transform $f\psi$, and 3) examine the decay of the Fourier transform in the direction $\xi_0$. Rapid decay of the Fourier transform in direction $\xi_0$ corresponds to smoothness of the function $f$ in the direction $\xi_0$ [59].

**Example: a point scatterer** If $f(r) = \delta(r)$, then

$$WF(f) = \{(0, \xi) : \xi \neq 0\}. \tag{13}$$

**Example: a line** Suppose $f(r) = \delta(r \cdot \nu)$. Then $WF(f) = \{(r, \alpha\nu) : r \cdot \nu = 0, \alpha \neq 0\}$.

Microlocal analysis can be used in two main ways for feature identification:

1. One can use microlocal analysis to determine how features of the scene correspond to singularities in the data space. Features in the scene can often then be identified directly from the data. [11, 56]

2. One can form an image and use microlocal analysis to determine how singularities in the scene correspond to singularities in the image. Features of the scene can then be identified from features in the image. [6, 49, 50]

### 3.2 Features in the data

To illustrate the first approach, we note that in the infinite-bandwidth case, (12) is of the form of a Fourier Integral Operator (FIO) [30] applied to $Q$. The phase of an FIO determines how it maps wavefront sets. In particular, the mapping between wavefront sets is determined by a set in phase space called the *canonical relation*. This set is determined by the phase of the FIO, which in the case of point scatterers is the phase of (12):

$$\phi(\omega, t, r, r') = -\omega(t - 2|r - r'|/c). \tag{14}$$

In this case, the canonical relation is

$$\begin{aligned} \Lambda &= \{\big((t, r; \tau, \sigma), (r', \xi)\big) : d\phi/d\omega = 0, \sigma = d\phi/dr, \tau = d\phi/dt, \xi = -\nabla_{r'}\phi\} \\ &= \Big\{ \big((t, r; \tau, \sigma), (r', \xi)\big) : t = 2|r - r'|/c, (\sigma, \tau) = \omega \left(2\omega(\widehat{r - r'})/c, 1\right), \\ &\quad \zeta = 2\omega(\widehat{r - r'})/c \Big\}. \end{aligned} \tag{15}$$

The wavefront set of the radar measurements $d$ is obtained as the set of points $(t, r; \tau, \sigma)$ for which there is a corresponding $(r', \xi)$ in the wavefront set of $V$.

Identification of the wavefront set of the data can, in many cases, be used to identify the wavefront set of the reflectivity function $V$ and thus to identify features in the scene.

Practical numerical methods for computing the wavefront set of data, however, are in their infancy. The problem is closely related to the problem of detecting edges in images.

### 3.3 Features in the image

In the second approach, we first form an image from the data using a backprojection or matched filtering algorithm:

$$I(r) = \int_{\mathbb{R}^3 \times \mathbb{R}} e^{i\omega(t - 2|r - r''|/c} Q(t, r'', \omega) d\omega D(r'', t) dr'' dt \tag{16}$$

where $Q$ is to be determined below.

We plug in expression (12) for the data and do the $t$ integration:

$$I(r) \sim \int_{\mathbb{R}\times\mathbb{R}^3\times\mathbb{R}^3} e^{i2\omega(|r-r''|-|r''-r'|)/c} QA(t, r'', \omega)V(r'')\ d\omega dr'' dr.' \tag{17}$$

This is of the form $I(r) = \int_{\mathbb{R}^3} K(r, r')V(r')dr'$ where

$$K(r, r') = \int_{\mathbb{R}\times\mathbb{R}^3} e^{i2\omega(|r-r''|-|r'-r''|)/c} QA(2|r - r''|/c, r'', \omega)d\omega dr'' \tag{18}$$

is the point spread function. We want $K$ to look like a delta function

$$\delta(r - r') = \int_{\mathbb{R}^3} e^{i(r-r')\cdot\xi} d\xi. \tag{19}$$

The main contribution to (18) comes from the **critical points**

$$\begin{aligned} |r - r''| &= |r' - r''| \\ \nabla_{r''}|r - r''| &= \nabla_{r''}|r' - r''| \end{aligned} \tag{20}$$

If $K$ is to look like the delta function (19), then we want critical points only when $r = r'$. Extraneous critical points can cause artifacts in the image. Whether such extraneous critical points are present or not depends on the measurement geometry and on the antenna beam pattern $A$.

In the neighborhood of critical points $r = r'$, the following approach was suggested by G. Beylkin [6] . Since we want the exponent of (18) to look like $(r - r') \cdot \xi$, we should do a Taylor expansion of exponent around the point $r = r'$. This results in

$$2\omega(|r - r''| - |r' - r'')|)/c = (r - r') \cdot \Xi(r, r', r'', \omega) \tag{21}$$

where near $r = r'$, $\Xi(r, r', r'', \omega) \approx (2\omega/c)\widehat{r - r'}$. We then make the change of variables

$$(r', \omega) \to \xi = \Xi(r, r', r'', \omega) \tag{22}$$

in (18), which results in

$$K(r,r') = \int_{\mathbb{R}^3} e^{i(r-r')\cdot\xi} Q A(r,r',\omega) \left| \frac{\partial(r',\omega)}{\partial\xi} \right| d\xi \tag{23}$$

The Jacobian determinant $\left|\frac{\partial(r',\omega)}{\partial\xi}\right|$ is called the **Beylkin determinant**.

¿From comparing (23) with (19), we see that we should take $Q = 1/(A\ |\partial(r',\omega)/\partial\xi|)$. With this choice, the point spread function is

$$K(r-r') = \int_{\mathbb{R}^3} e^{i(r-r')\cdot\xi} \chi(r',\xi) \left| \frac{\partial(x,\omega)}{\partial\xi} \right| d\xi \tag{24}$$

where $\chi$ is a characteristic function that is one over regions corresponding to the measurement aperture and zero for regions in which there is no data. A smooth taper should be included in $\chi$ to avoid artifacts due to edges of the data collection region.

The formula (24) exhibits $K$ as the kernel of a **pseudodifferential operator**, i.e., an FIO with the same phase as the delta function (19). Pseudodifferential operators have the desirable *pseudolocal property* [59], which is that they cannot increase the wavefront set. In this context, since $I = KV$, this means that the wavefront set of the image is equal to, or is a subset of, the wavefront set of the reflectivity function $V$. In other words, the image contains no singularities that are due to artifacts.

If the viewing aperture is limited, it is possible that edges that are present in $V$ might not appear in the image $I$. However, we are guaranteed that all edges in the image $I$ do correspond to singular features of $V$. Thus we can expect to identify features of $V$ from the image $I$.

# 4 Parametric Shape-Based Methods

In addition to the analytically-oriented approach to feature-enhanced inversion discussed in the previous section, we are actively pursuing research on alternate, more parametric approaches to these problems. In a variety of applications as opposed to the highly structured man-made targets of interest in the case of SAR imaging, one is directly concerned with characterizing well-localized,

amorphously shaped anomalies present in a perhaps unknown or partially known background. Moreover, the simplifying assumptions concerning the sensing scenario which allowed for the detailed analysis of § 3 may be absent. For example

1. A linearized physical model may not be sufficiently accurate for inversion so that a fully non-linear inverse problem must be solved

2. The map from medium to data may be smoothing to such an extent that singularities in the medium are not (stably) recoverable.

3. Should the anomaly-free background not be free space, but rather a lossy and inhomogeneous medium, the simple Green's function which was at the heart of the microlocal methods is replaced by a far less tractable function making analysis all the more difficult.

While these complicating factors do not preclude the development of elegant and useful microlocal or other analytical approaches (see [11] for some recent work in these areas), they certainly do make such work far more difficult and less easy to apply for processing data from real sensing systems. Motivated in part by these issues, our group has considered a more direct approach to localizing blob-like anomalies in sensing problems for which the physics offer little simplification.

The approach we have taken is to consider models for the anomaly and perhaps the background that are explicitly parameterized by the quantities of interest: size, shape, location, and contrasts. Given data from a sensing system, an optimization problem is solved to determine that set of parameters which produces a shape which best fits the data. Here in fact, we consider a simple square error criterion of the form:

$$\mathcal{E}(\theta) = \frac{1}{2} \sum_{i=1}^{M} \sum_{j=1}^{N} \left| w_{ij} (\phi^i(\mathbf{r}_j; \theta) - \phi^i_{\text{obs}}(\mathbf{r}_j)) \right|^2 . \tag{25}$$

where $\phi^i(\mathbf{r}_j; \theta)$ is the hypothesized response due to source $i$ at detector $j$, and is a function of a vector of parameters, $\theta$ describing the shape and contrast of the anomaly. In (25) $\phi^i_{\text{obs}}(\mathbf{r}_j)$ is the observed response and $w_{ij}$ represents a weighting function.

We have found that the use of these very low order models (i.e. the vector $\theta$ contains few parameters) leads to inversion schemes which are more efficient and robust than typical pixel-based methods. Essentially, these models have the effect of regularizing the inversion problem. The simplicity of this class of methods does come at a (small) price. First, for the approaches we discuss in this paper, it is necessary to know the number of objects in the medium under investigation. For many problems one may safely assume this number to be one. When this is not the case, this order determination problem remains an open one for us; although one for which well known techniques may be applied. A second issue is the richness of the solution offered. By using only simple parametric shapes such as spheres and ellipsoids, it is clear we can hope only to roughly characterize the detailed shape of the anomalies. In low-resolution applications such as DOT and ERT, this may well be the finest level of detail supported by the data. Alternatively, one could consider our approach as providing a very good initial guess for other, more intensive inversion schemes such as level set methods [29, 42].

In the remainder of this section, we discuss two different methods for solving the parametric shape optimization problem both in the context of diffuse optical tomography (DOT). In § 4.1, a Gauss-Newton type of optimization approach based on the integral equation formulation of the physics is employed to estimate the parameters of an ellipsoid-shaped inclusion in the tissue optical properties. Alternatively, a PDE formulation is used as the basis for an adjoint-field approach to fitting a spherical shape again to an absorption anomaly in § 4.2. The results presented are meant to provide a preliminary demonstration as to the potential utility of this class of methods for problems such as DOT. They are not meant to be the final word on the issue. Indeed, a major focus of our work in the coming years is the evaluation of the "lessons learned" from pursuing these varying algorithmic strategies and shape models to arrive at a more coherent means of determining the correct model/algorithm pair for a given application.

## 4.1 A Gauss-Newton Approach to Ellipsoid Optimization

The goal of this work has been the development of methods for characterizing anomalies in the space-varying optical absorption coefficient, $\mu_a(r)$[2], when the background may not be completely known. To begin, we assume for a moment that the boundary of the anomaly is known. Then we can define $S(r)$ as the characteristic function

$$S(r) = \begin{cases} 1 & r \in \text{anomaly} \\ 0 & \text{otherwise} \end{cases}$$

Next, we assume that the value of the perturbation at a point in the background tissue can be expressed in as the linear combination of a small number, say $N_b$, of known basis functions. We assume the same about the value inside the anomaly, although the number, $N_a$ of basis functions and the type may be different [35]. We now define the value of the perturbation function at the point $r$ according to

$$\mu_a(r) = S(r)\underbrace{B_1(r)}_{1\times N_a}\overbrace{\alpha}^{N_a\times 1} + [1 - S(r)]\underbrace{B_2(r)}_{1\times N_b}\overbrace{\beta}^{N_b\times 1}.$$

Notice that $B_1(r)$ (likewise $B_2(r)$) is a row vector whose columns are the values of the anomaly (background) basis functions at $r$, and the components in $\alpha$ ($\beta$) are the expansion coefficients.

Upon discretization, the equation becomes

$$\mu_a = SB_1\alpha + (I - S)B_2\beta \tag{26}$$

where $S$ now represents a diagonal $n \times n$ matrix with 1's and 0's on the diagonal, $I$ denotes the identity matrix of the same size and

$$B_1 \in R^{n\times N_a}, \qquad B_2 \in R^{n\times N_b}$$

$$\alpha \in R^{N_a}, \qquad \beta \in R^{N_b}.$$

[2]Recall from§ 2 that $\mu_a$ enters problem via the squared wavenumber, $k^2$.

Thus, if $S$ is known, there are a total of $N_a+N_b$ unknowns that we need in order to define $g$. The idea is then to implicitly define $S$ in terms of a small number of unknowns. For two dimensional problems, describing the boundary in terms of a b-spline basis proved useful [35, 46]. For three dimensional problems of current interest to us, shapes such as spheres or ellipsoids are sufficient, and these ideas are presented below.

We begin by characterizing an ellipsoid as in [36], and consider the sphere as a special case. To completely characterize an ellipsoid, we need only the lengths of the semi-axes contained in a 3-length vector $v$, a centroid location contained in a 3-length vector $c$, and a set of orthogonal basis vectors describing the orientation of the axes which can be implicitly defined in terms of a 3-length vector of Euler angles, say $\theta$. This leads to a total of 9 unknowns that must be determined to find an ellipsoid. If the object is assumed to be a sphere, $v$ becomes a scalar and the $\theta$ vector is not needed, leaving a total of 4 unknowns that must be determined.

Given the preceding discussion and our model, the 3D "inverse" problem, in the case of ellipsoids, becomes

$$\min_{\alpha,\beta,c,v,\theta} \|W(d - h(\alpha, \beta, c, v, \theta))\|_2^2, \tag{27}$$

where $d$ represents the measured data vector stacked over all sources, $h$ represents the nonlinear forward operator, and $W$ is a diagonal weighting matrix used to whiten the data. In the special case of spheres, the optimization problem further simplifies to

$$\min_{\alpha,\beta,c,v} \|W(d - h(\alpha, \beta, c, v))\|, \tag{28}$$

where $v$ is scalar.

Notice that we have reduced the search space considerably: instead of optimizing over $R^n$, we are optimizing over the $N_a+N_b$ entries in $\alpha$ and $\beta$ and the 9 entries in the vectors $c, v, \theta$ (or 4 entries in the spherical case). In [36], an integral equation formulation is used for the forward problem and the inverse problem is solved via a modified Gauss-Newton approach. In that work, the authors illustrated through experiments that this method can provide useful results for very limited data.

#### 4.1.1 Example 1: Sphere

The true values, initial guesses, and final estimates of all relevant parameters for the problem are shown in Table 2. Here, we have taken $N_b = 3$. The columns of $B_2$ are generated as

$$B_2 = [\sin(3x) + 1, \cos(8y). * \sin(2y) + 1, \sin(5z) + 1].$$

We note that the background perturbation was found to have a maximum of 9.97e-3, a minimum of 1.74e-5, and an average value of 4.96e-3. The initial sphere was the largest such structure, with centroid at the center of the region of interest (ROI), that would fit inside the ROI, namely, a sphere of radius 2 cm, centered at $x = 0, y = 0, z = 3$. Initial guesses for $\alpha$ and $\beta$ were based on a separate Gauss-Newton solve holding the sphere/ellipsoidal parameters fixed. For more information on how we obtained starting guesses for $\alpha$ and $\beta$, see [36].

To illustrate the promise of our inversion approach, the $B_2$ used in the reconstruction was the same as that for the true image; however in [36] it is shown that it is possible to reconstruct using a mismatched model with varying degrees of success. The starting guess at the sphere was the largest sphere, with centroid at the center of the region of interest, that would fit inside the region of interest, namely, a sphere of radius 2 cm, centered at $x = 0, y = 0, z = 3$.

These recovered parameter values in Table 2 lead to a final estimate of $S$ having only a 12 voxel mismatch. Thus, by correctly modeling the background perturbations, we can obtain a significant improvement in localization and in the estimated value of $\alpha$. Figure 2 shows slices in height $z$ of the reconstruction. The colormap used in Figure 2 is the same as the colormap used in Figure 5.

#### 4.1.2 Example 2

Now we specify a "lumpy" background for the true image using $N_b = 3$ and $B_2 = [sin(\omega x) + 1, sin(\zeta y) + 1, sin(\kappa z) + 1]^T$, with $\omega = 7; \zeta = 3; \kappa = 4$. This gives a max background perturbation value of $1.20e - 2$, a minimum perturbation value of $3.07e - 5$ and an average of $5.98e - 3$.

Table 3 provides the true values and estimations results for the object and background in this experiment. Slices of the true background perturbation at various depths are given in Figure 3.

Note that different angles can affect essentially the same rotation (i.e. the $\theta_i$ are not unique), so we report them only for completeness (the Figure illustrates our algorithm did very well determining the correct rotation). There was only a 21 voxel mismatch. The value inside the anomaly is slightly too small and is due to the fact that the reconstructed anomaly is slightly too big (overestimating the size and underestimating the value inside the anomaly go hand in hand). Cross-sections in height $z$ are illustrated in Figure 4.

### 4.2 Adjoint Field Methods for Determining Best-Fit Spheres

As an alternate to the work in [36, 46] in which a Gauss-Newton optimization approach based on an integral equation form of the diffusion model was used to determine the structure of an ellipsoidal shape as well as the "texture" coefficients, we have also recently been exploring the use of gradient-type of adjoint-field methods based on the underlying PDE for solving shape-based inverse problems. The Gauss-Newton method converges at a faster rate than a steepest descent of non-linear conjugate gradient approach. However, computation with the integral equation nominally requires the storage and manipulation of large dense matrices for solving the forward problem. The PDE-based method requires only sparse-matrix storage and manipulation. One area of future work in our group is to examine in more detail the tradeoffs inherent in these choices and perhaps devising new methods which combine the best of each approach.

To begin our overview of the adjoint field method, we note that a key element of any gradient-based algorithm (e.g. steepest descent or non-linear conjugate gradient) for minimizing $\mathcal{E}$ in (25) is the efficient computation of the functional gradient, or Fréchet derivative, of $\mathcal{E}$ with respect to a change in $\mu_a(r)$. As shown in [51] this can be accomplished as $\nabla_{\mu_a(r)}\mathcal{E}(r) = \sum_{i=1}^{M} \mathrm{Re}\left[\tilde{\phi}^i(r)\phi^i(r)\right]$ where $\tilde{\phi}^i(r)$, the adjoint field due to source $i$, satisfies the adjoint PDE:

$$-\nabla \cdot \nabla\sigma(r)\tilde{\phi}^i(r) + (\mu_a(r) + \frac{j\omega}{c})\tilde{\phi}^i(r) = \tilde{s}(r) \tag{29}$$

where the adjoint source is defined by

$$\tilde{s}(r) = \sum_{j=1}^{N} \left[ w_{ij}(\phi^i(r_j) - \phi^i_{\text{obs}}(r_j)) \right]^* \delta(r - r_j) \tag{30}$$

with $v$ the speed of light in the medium. In a sense, (29) indicates that, for each source, we compute $\tilde{\phi}^i(r)$, by propagating the complex conjugate of the weighted error at the receivers into the medium. Using the functional derivative, we can iteratively minimize our error measure, (25), by means of standard optimization methods, such as the nonlinear conjugate gradient algorithm. The primary advantage of the adjoint field method is that we can compute the Fréchet derivative by computing a single forward solve for each source; this is a large saving compared to the use of finite differences to approximate the gradient for each degree of freedom in the reconstruction.

Our primary interest in the adjoint field approach has been in the context of parametric, shape-based inversion schemes. We have concentrated on the problem of determining the size and location of an absorption anomaly which is assumed to take the form of a sphere with center $(x_o, y_o, z_o)$, radius $r$ and $\mu_a^o$ in a known background $\mu_a^b$:

$$\mu_a(r) = \mu_a^b(r) + (\mu_a^o(r) - \mu_a^b(r))H(O(r)) \tag{31}$$
$$O(r) = r^2 - (x - x_o)^2 - (y - y_o)^2 - (z - z_o)^2$$

In the above, $H(r)$ is the Heaviside step function, and $O(r)$ is the object shape function.

The gradient of the error with respect to a parameter $p$ of $O(r)$ is:

$$\frac{\partial \mathcal{E}}{\partial p} = \int_{\mathbb{R}^3} \text{Re}(\sum_{i=1}^{M} \tilde{\phi}^i(r)\phi^i(r))\delta(O(r))\frac{\partial O(r)}{\partial p} d^3r \tag{32}$$

For example, for the spherical object function, the gradient of the error with respect to $x_o$ is:

$$\frac{\partial \mathcal{E}}{\partial x_o} = \int_{\mathbb{R}^3} 2(x - x_o)\delta(O(r))\nabla_{\mu_a(r)}\mathcal{E} d^3r \tag{33}$$

### 4.2.1 Examples

As an example, we consider the case of determining the location, radius, and contrast of a spherical absorbing inhomogeneity within a cube with dimensions $6 \times 6 \times 6$cm. A reflection geometry is used, with sources and detectors interlaced on the $z = 0$ plane. The background absorption is $0.05\text{cm}^{-1}$, while that of the absorbing sphere is $0.3\text{cm}^{-1}$, and a value of $15\text{cm}^{-1}$ for $\mu_s$ was used.

We see in Fig. 5 and 6 that the absorber is characterized and located with fairly high accuracy. In Fig. 5 we show the progression of the estimates for the object center as function of algorithm iteration. We start from an initial point in the parameter space and, at each iteration, conduct a line search in the direction of the gradient to minimize the error function. In contrast, Fig. 7 shows a full nonlinear reconstruction of the absorption within the cube with regularization parameter 0.1. Here $\mu_a$ is estimated independently at 27000 voxel positions. In the absence of prior information about the form of the solution, the inversion poorly estimates the volume and the absorption of the inhomogeneity.

As a second example, we examine the utility of the approach for the processing of real data. The data were produced by an experimental apparatus at Massachusetts General Hospital (MGH). As illustrated in Figure 8(a), a transmission geometry is considered with 30 sources located at the $z = 0$ plane and a collection of nine receivers at the plane $z = 4.5cm$. Ground truth consisted of an absorbing sphere of radius 1 cm positioned in the center of a homogeneous background. The optical properties of the sphere are not known. Those of the background are $\mu_a = 0.023/\text{cm}$ and $\mu_{s'} = 10/\text{cm}$. The final result of the algorithm are shown in Figure 8(a) and in the the remaining subfigures we plot the error in the location, size, and contrast of the sphere. Clearly, these preliminary results indicate the potential utility of the method for real applications.

## 5 Conclusions and Future Work

In this paper, we have provided an overview of a number of feature-enhanced methods of use in limited-view, tomographic types of imaging problems. The underlying physics for all of our methods was captured in the frequency domain using a scalar Helmholtz equation or in the time domain, via

its wave equation counterpart. Two general classes of methods were considered. Microlocal analysis provided a powerful approach for using the limited data to obtain images in which objects' edges (or other discontinuities) are naturally enhanced. Preliminary results indicate that this method holds some promise for synthetic aperture radar imaging. For problems such as diffuse optical tomography or electrical resistance/impedance tomography, where the modeling assumptions underlying the microlocal work do not hold, we have discussed parametric, shape-oriented methods for estimating the structure of discrete anomalies located in a perhaps unknown background. These methods all revolved around the use of optimization procedures for determining the parameters governing the location, shape, orientation, and contrast of the unknown anomaly as well as the background.

Given the results and methods discussed here, a number of issues are immediately apparent for future work. First and foremost is the validation of these methods using real sensor data. In the medical imaging community for example, inverse problems associated with CAT, MRI, and to a lesser extent, ultrasound, are solved on a daily basis by practitioners all over the world. Such is not the case for the applications and the algorithms considered in this work. Obtaining high-quality, well-calibrated data (such as those used in § 4.2.1) which can be used to rigorously test the utility of these methods "in the field" requires as much if not more effort than the initial algorithm development itself. Thus, a key focus of our effort in the near future is to collaborate with practitioners across a number of fields to develop new methods for streamlining the process of algorithm validation and then to actually examine whether, in practice, these methods will be useful.

Additionally, we are actively pursuing the extension and merging of the methods contained in this paper as well as other under investigation. Using the microlocal techniques in conjunction with low-order-modeling methods such as those in § 4.1 to allow for edge-enhanced imaging in the presence of inhomogeneous background is another possibility. Finally, we are actively pursuing work in adjoint field methods for problems in which multiple ellipsoids might be required to adequately localize anomalies. Combining these techniques with other, non-parametric geometric inverse schemes such as level set methods may prove useful. Finally, dealing with problems in which localized anomalous behavior may be present in more than one physical parameter (e.g. op-

tical absorption and scattering in DOT) provides us with some interesting challenges in the area of feature-based inverse methods.

## References


[1] Richard A. Albanese, Richard L. Medina, and John W. Penn. Mathematics, medicine and microwaves. *Inverse Problems*, 10:995–1007, 1994.

[2] Simon Arridge. Optical tomography in medical imaging. *Inverse Problems*, 15:R41–R43, 1999.

[3] Murat Belge, Misha Kilmer, and Eric Miller. Wavelet domain image restoration with adaptive edge-preserbing regularization. *IEEE Trans. Image Processing*, 9(4):597–608, April 2000.

[4] M. Bertero and P. Boccacci. *Introduction to Inverse Problems in Imaging.* IOP, Bristol, 1998.

[5] G. Beylkin. Imaging of discontinuities in the inverse scattering problem by inversion of a causal generalized radon transform. *J. Math. Phys.*, 26:99–108, 1985.

[6] G. Beylkin. Imaging of discontinuities in the inverse scattering problem by inversion of a causal generalized radon transform. *J. Math. Phys.*, 26:99–108, 1985.

[7] D. A. Boas. A fundamental limitation of linearized algorithms for diffuse optical tomography. *Optics Express*, 1(13), 22 December 1997.

[8] Brett Borden. *Radar Imaging of Airborne Targets: A Primer for Applied Mathematicians and Physicists.* IOP, 1999.

[9] M. Cetin and W. C. Karl. Feature-enhanced synthetic aperture radar image formation based on non-quadratic regularization. *IEEE Trans. Image Processing*, 10(4):623–631, April 2001.

[10] M. Cheney. A mathematical tutorial on synthetic aperture radar. *SIAM Review*, 43:301–312, 2001.

[11] M. Cheney and B. Borden. The structure of radar data for range-doppler imaging. preprint.

[12] M. Cheney, D. Isaacson, and M Lassas. Optimal acoustic measurements. *SIAM J. Appl. Math.*, 61:1628–1647, 2001.

[13] Margaret Cheney. The linear sampling method and the MUSIC algorithm. *Inverse Problems*, 17:591–595, 2001.

[14] Margaret Cheney. A mathematical tutorial on synthetic aperture radar. *SIAM Review*, 43:301–312, 2001.

[15] Margaret Cheney. Tomography prolems arising in synthetic aperture radar. In E. T. Quinto, L. Ehrenpreis, A. Faridani, and F. Gonzalezand E. Grinberg, editors, *Radon Transforms and Tomography*. American Math. Soc., Providence, R. I., 2001.

[16] Margaret Cheney, David Isaacson, and Jonathan C. Newell. Electrical impedance tomography. *SIAM Review*, 41(1):85–101, 1999.

[17] W.C. Chew and Y. M. Wang. Reconstruction of two-dimensional permittivity distribution using the distorted born iterative method. *IEEE Trans. Medical Imaging*, 9(2):218–225, June 1990.

[18] Weng Cho Chew. *Waves and Fields in Inhomogeneous Media*. Van Nostrand Reinhold, New York, 1990.

[19] Chien-Ching Chiu and Yean-Woei Kiang. Inverse scattering of a buried conducting cylinder. *Inverse Problems*, 7:187–202, 1991.

[20] Chien-Ching Chiu and Yean-Woei Kiang. Electromagnetic inverse scattering of a conducting cylinder buried in a lossy half-space. *IEEE Trans. on Antennsa and Propagation*, 40(12), Augusts 1992.

[21] David Coltin and Rainer Kress. *Inverse Acoustic and Electromagnetic Scattering Thoery*, volume 93 of *Applied Mathematical Sciences*. Springer-Verlag, 1992.

[22] David Colton, Klaus Giebermann, and Peter Monk. A regularized sampling method for solving three-dimensional inverse scattering problems. *SIAM J. Scientific Computing*, 21(6):2316–2330, 2000.

[23] David Colton and Peter Monk. A modified dual space method for solving the electromagnetic inverse scattering problem for an infinite sylinder. *Inverse Problems*, 10:87–107, 1994.

[24] David Colton and Peter Monk. A linear sampling method for the detection of leukemia using microwaves. *SIAM J. on APplied Mathematics*, 58(3):926–941, 1998.

[25] Y. Das, J. E. McFee, J. Toews, and G. C. Stuart. Analysis of an electromagnetic induction detector for real-time localization of buried objects. *IEEE Trans. on Geoscience and Remote Sensing*, 28:278–287, May 1990.

[26] R. Deming and A. J. Devaney. A filtered backpropagation algorithm for GPR. *Journal of Environmental and Engineering Geophysics*, 0(2):113–123, January 1996.

[27] Guy Demoment. Image reconstruction and restoration: Overview of common estimation structures and problems. *IEEE Trans on ASSP*, 37(12):2024–2036, 1989.

[28] A. J. Devaney. Reconstructive tomography with diffracting wavefields. *Inverse Problems*, 2:161–183, 1986.

[29] Oliver Dorn, Eric L. Miller, and Carey Rapaport. A shape reconstruction method for electromagnetic tomography using adjoint fields and level sets. *Inverse Problems*, 16(5):1119–1156, October 2000. invited paper.

[30] J. J. Duistermaat. *Fourier Integral Operators*. Birkhauser, Boston, 1996.

[31] A. Grigis and J. Sjöstrand. *Microlocal Analysis for Differential Operators: An Introduction*, volume 196 of *London Mathematical Society Lecture Note Series*. Cambridge University Press, 1994.

[32] Houssem Haddar and Peter Monk. The linear sampling method for solving the electromagnetic inverse medium problem. *Inverse Problems*, 18:891–906, June 2002.

[33] Avinash C. Kak and Malcolm Slaley. *Principles of Computerized Tomographic Imaging*. IEEE Press, Piscataway, N.J., 1987.

[34] W. C. Karl, G. C. Verghese, and A. S. Willsky. Reconstucting ellipsoids from projections. *Computer Vision, Graphics, and Image Processing: Graphical Models and Image Processing*, 56(2):124–139, March 1994.

[35] Misha Kilmer, Eric Miller, David Boas, and Dana Brooks. A shape-based reconstruction technique for DPDW data. *Optics Express*, 7(13):481–491, December 18 2000.

[36] Misha E. Kilmer, Eric L. Miller, David Boas, and Alethea Barbaro. 3d shape-based imaging for diffuse optical tomogrpahy. *Applied Optics*, 2002.

[37] R. E. Kleinman and P. M. van den Berg. An extended range-modifed gradient technoque for profile inversion. *Radio Science*, 28(5):877–884, September-October 1993.

[38] Jin Au Kong. *Electromagnetic Fields*. John Wiley and Sons, 1986.

[39] G. Kristensson and C. R. Vogel. Inverse problems for acoustic waves using the penalalized likelihood method. *Inverse Problems*, 2:461–479, 1986.

[40] S. Osher L. I. Rudin and E. Fatemi. Nonlinear total variation based noise removal algorithms. *Phys. D*, 60:259–268, 1992.

[41] D. J. LaBrecque, M. Milletto, W. Daily, A. Ramirez, and E. Owen. The effects of noise on Occam's inversion of resistivity tomography data. *Geophysics*, 61:538–548, 1996.

[42] A. Litman, D. Lesselier, and F. Santosa. Reconstruction of a two-dimensional binary obstacle by controlled evolution of a level-set. *Inverse Problems*, 14:685–706, 1998.

[43] Andeas Mandelis, Frank Funak, and Mahendra Munidasa. Generalized methodology for thermal diffusivity depth profile reconstruction in semi-infinite and finitely thick inhomogenous solids. *J. Appl. Phys.*, 80(10):5570–5578, 15 Nov. 1996.

[44] Andreas Mandelis. *Diffusion Wave-Fields*. Springer-Verlag, New York, 2001.

[45] Peyman Milanfar, William C. Karl, and Alan S. Willsky. Reconstructing binary polygonal objects from projections: A statistical view. *CVGIP: Graphical Models and Image Processing*, 56(5):371–391, September 1994.

[46] Eric L. Miller, Misha E. Kilmer, and Carey M. Rappaport. A new shape-based method for object localization and characterization from scattered field data. *IEEE Trans. on Geoscience and Remopte Sensing*, 38(4):1682–1696, July 2000. invited paper.

[47] Eric L. Miller, Lena Nicolaides, and Andreas Mandelis. Nonlinear inverse scattering methods for thermal wave slice tomography: A wavelet domain approach. *Journal of the Optical Society of America (A)*, 15(6):1545–1556, June 1998.

[48] Walter Munk and Carl Wunch. Ocean acoustic tomography: A scheme for large scale monitoring. *Deep Sea Research*, 26A:123–161, 1979.

[49] C. J. Nolan and M. Cheney. Synthetic aperture inversion. *Inverse Problems*, 18:221–236, 2002.

[50] C. J. Nolan and W. W. Symes. Global solution of a linearized inverse problem for the acoustic wave equation. *Comm. in P.D.E.*, 22(5–6), 1997.

[51] Stephen J. Norton. Iterative inverse scattering algorithms: Methods of computing Frechet derivatives. *Journal of the Acoustic Society of America*, 106:2653, 1999.

[52] M. A. O'Leary, D. A. Boas, B. Chance, and A. G. Yodh. Reactio of diffuse photon density waves. *Physical Review Letters*, 69(18), 2 November 1992.

[53] M. A. O'Leary, D. A. Boas, B. Chance, and A. G. Yodh. Experimental images of heterogeneous turbid media by frequency-domain diffusing-phton tomographt. *Optics Letters*, 20(5), March 1 1995.

[54] Mutafa Ozdemir, Eric L. Miller, and Stephen J. Norton. Localization and characterization of buried objects from multi-frequency, array inductive data. In Abinash C. Dubey, James F. Harvey, J. Thomas Broach, and Regina E. Dugan, editors, *Proc. SPIE AeroSense Symp.* ,

*Detect. Technologies for Mines and Minelike Targets IV*, volume 3710, pages 26–36. SPIE, April 1999.

[55] Joseph P. et al. Pickett, editor. *The American Heritage Dictionary of the English Language.* Houghton Mifflin Co., Boston, forth edition, 2000. http://www.bartleby.com/61/.

[56] E. T. Quinto. Singularities of the X-ray transform and limited data tomography in $r^2$ and $r^3$. *SIAM J. Math. Anal.*, 24:1215–1225, 1993.

[57] David J. Rossi and Alan S. Willsky. Reconstruction from projections based on detection and estimation of objects–parts I and II: Performance analysis and robustness analysis. *IEEE Trans. on ASSP*, ASSP-32(4):886–906, August 1984.

[58] Andrea Tacchino1, Joe Coyle, and Michele Piana. Numerical validation of the linear sampling method. *Inverse Problems*, 18:511–527, June 2002.

[59] F. Treves. *Introduction to Pseudodifferential and Fourier Integral Operators*, volume I and II. Plenum Press, New York, 1980.

[60] C. R. Vogel. *Computational Methods in Inverse Problems.* SIAM, Providence, 2002.

[61] C. R. Vogel and M. E. Oman. Fast, robust total variation-based reconstruction of noisy, blurred images. *IEEE Trans. Image Process.*, 7(7):813–824, July 1998.

[62] Alan Witten, I. J. Won, and Stephen J. Norton. Imaging underground structures using broadband electromagnetic induction. *Journal of Environmental and Engineering Geophysics*, 1(2):105–114, Sept. 1997.

[63] Alan Witten, I. J. Won, and Stephen J. Norton. Subsurface imaging with broadband electromagnetic induction. *Inverse Problems*, 13:1621–1639, 1997.

[64] R. Yarlagadda, J. B. Bednar, and T. L. Watt. Fast algorithms for LP deconvolution. *IEEE Trans. Acoustic, Speech and Signal Processing*, ASSP-33:174–181, 1984.

[65] J. Zhang, R. L. Mackie, and T. R. Madden. 3-D resistivity forward modeling and inversion using conjugate grdients. *Geophysics*, 60:1313–1325, 1995.

Table Captions

1. Problem and Sensor Characteristics
2. Estimation results for Sphere Recovery Example
3. Estimation results for Ellipsoid Recovery Example

Figure Captions

1. True image for example 1, slices in depth from left to right and top to bottom. Colormap is truncated to show the background variation (units are in 1/cm) so the anomaly with a value of .15 1/cm appears in bright white.
2. Reconstructed image for example 1. The colormap used is the same as for the true image. The reconstructed anomaly has a value of .168 1/cm.
3. True image for example 2, slices in depth from left to right and top to bottom. Colormap is truncated to show the background variation (units are in 1/cm) so the anomaly with a value of .15 1/cm appears in bright white.
4. Reconstructed image for example 2. The colormap used is the same as for the true image. The reconstruced anomaly has a value of .13 1/cm.
5. Center of hypothesized absorber at each iteration
6. Hypothesized $r$ and $\mu_a$ at each iteration
7. Regularized nonlinear inversion and true solution
8. Results of processing with real data

| Application Domain | Problem Areas | Modalities |
|---|---|---|
| **Medical Imaging** | - Tumor localization and characterization<br>- Functional imaging<br>- Drug Development | - Diffuse optical<br>- Acoustic<br>- Electrical Impedance |
| **Nondestructive evaluation** | - Crack and flaw detection<br>- Semiconductor or steel depth profiling | - Ultrasonic<br>- Electromagnetic induction<br>- Photo-thermal<br>- Photo-acoustic |
| **Military** | - Landmine detection<br>- Buried facility characteriization<br>- Airborne and satellite surveillance of foliage obscured objects | - Airborne SAR<br>- Ground penetrating radar<br>- Acoustic<br>- Electromagnetic induction |
| **Geophysics** | - Environmental monitoring<br>- Environmental remediation<br>- Oil and mineral exploration | - Seismic<br>- Electromagnetic induction<br>- Electrical impedance<br>- Electrical resistance<br>- Borehole radar |

Table 1:

| Parameter | Initial guess | Final estimate | True Value |
|---|---|---|---|
| $\alpha$ | .007 | 0.168 | N/A |
| $\beta$ | (.002,.0007,.003) | (0.002, 0.002, 0.001) | (.002, .002, .001) |
| Center (cm) | (0,0,3) | (-0.600, 0.999, 3.390) | (-0.6,1.0,3.4) |
| Radius (cm) | 2 | 0.755 | 0.800 |

Table 2:

| Parameter | Initial guess | Final estimate | True Value |
|---|---|---|---|
| $\alpha$ | 0.007 | 0.130 | N/A |
| $\beta$ | (0.003,0.002,-4.41e-6) | (0.002, 0.001, 0.003) | N/A |
| Center (cm) | (0,0,3) | (0.69, -0.91, 2.41) | (0.7, -0.9, 2.4) |
| Semi-axes (cm) | (3, 2.9, 2) | (0.824, 1.1, 0.531) | (1.1, 0.5, 0.8) |
| Rotation angles (rad) | 2 | (0.531, -1.49, 0.78) | $(\pi/4, \pi/4, 0)$ |

Table 3:

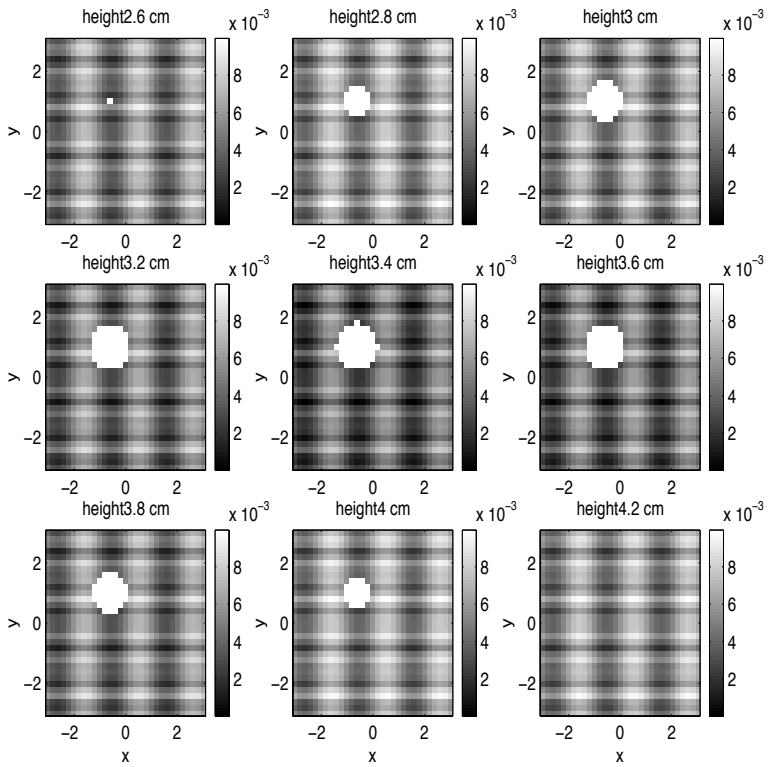
height2.6 cm
height2.8 cm
height3 cm
height3.2 cm
height3.4 cm
height3.6 cm
height3.8 cm
height4 cm
height4.2 cm
x 10^-3
y
x

Figure 1:

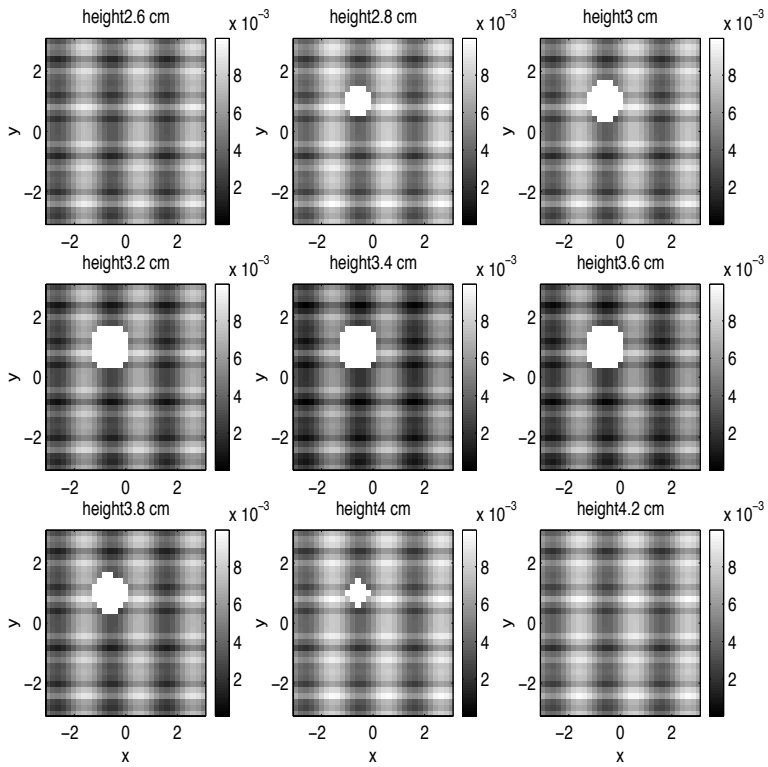
height2.6 cm
height2.8 cm
height3 cm
height3.2 cm
height3.4 cm
height3.6 cm
height3.8 cm
height4 cm
height4.2 cm
x 10^-3
x
y

Figure 2:

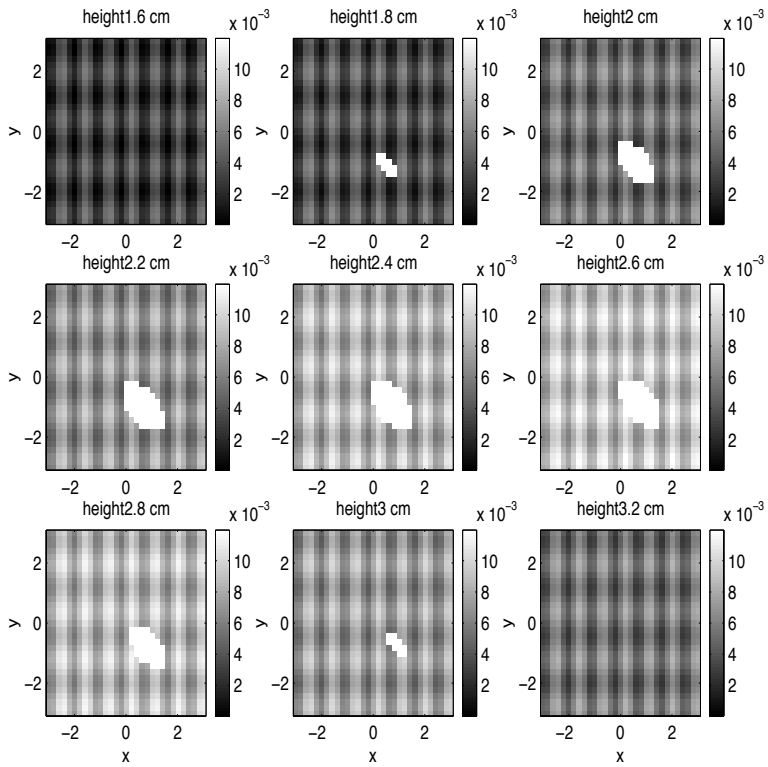
height1.6 cm
height1.8 cm
height2 cm
height2.2 cm
height2.4 cm
height2.6 cm
height2.8 cm
height3 cm
height3.2 cm
x 10^-3
y
x

Figure 3:

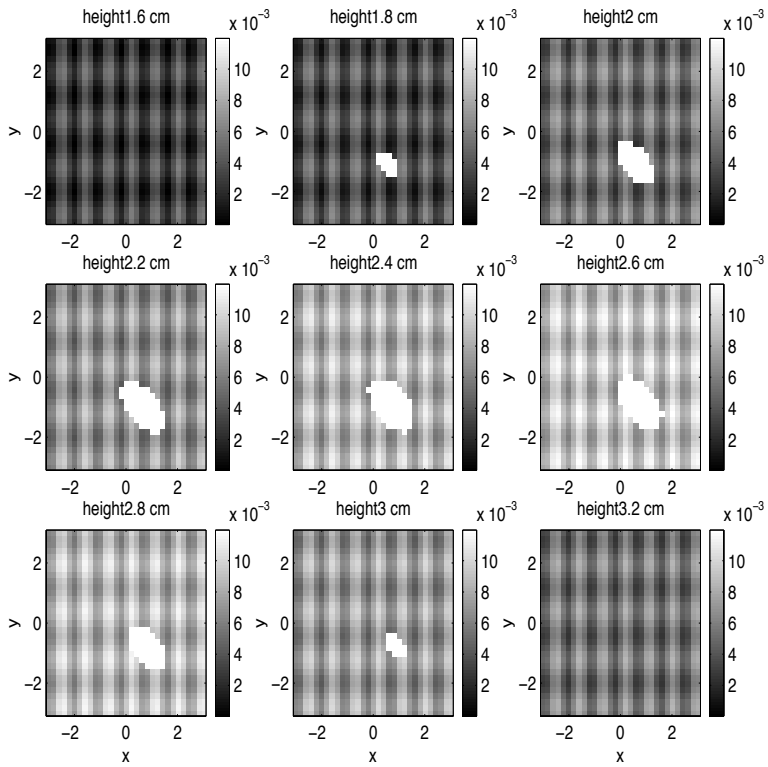
height1.6 cm
height1.8 cm
height2 cm
height2.2 cm
height2.4 cm
height2.6 cm
height2.8 cm
height3 cm
height3.2 cm
x 10^-3
x
y

Figure 4:

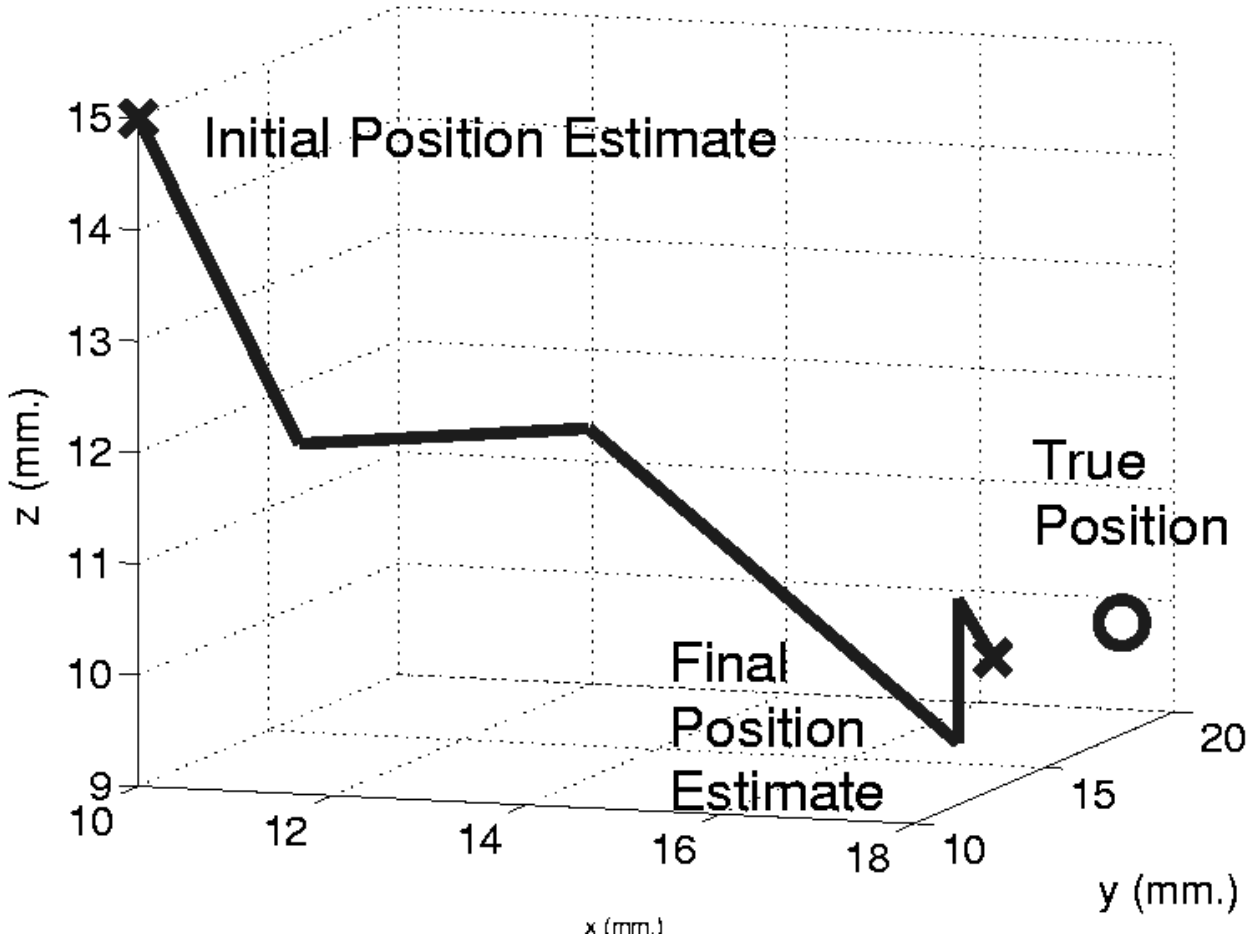
Initial Position Estimate
True
Position
Final
Position
Estimate
z (mm.)
15
14
13
12
11
10
9
10
12
14
16
18
x (mm.)
10
15
20
y (mm.)

Figure 5:

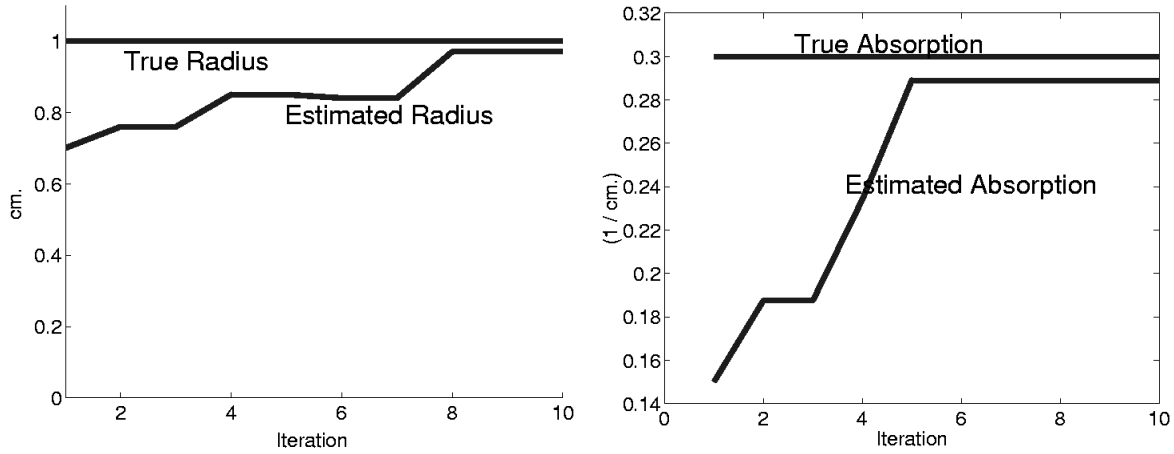
True Radius
Estimated Radius
cm.
Iteration
True Absorption
Estimated Absorption
(1 / cm.)
Iteration

Figure 6:

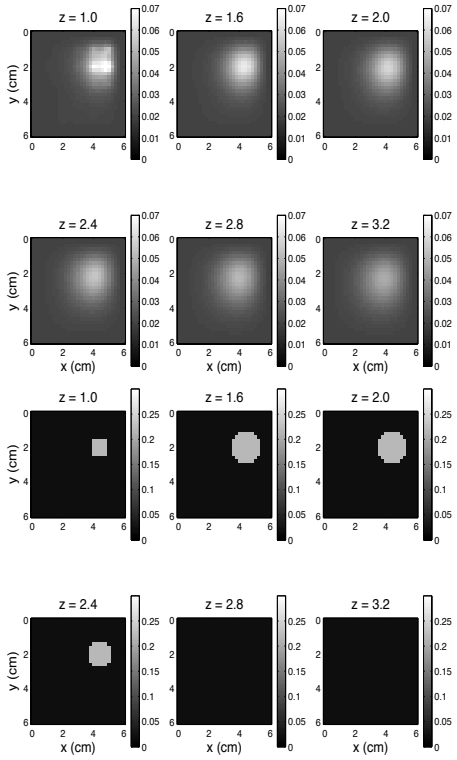


Figure 7:

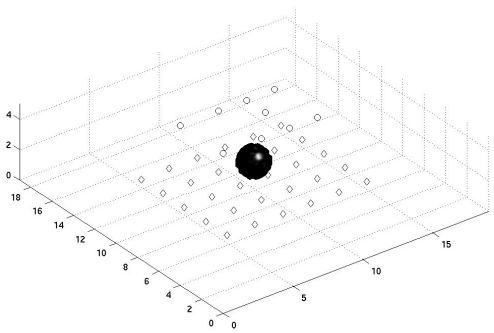

(a) Localization results for real data example

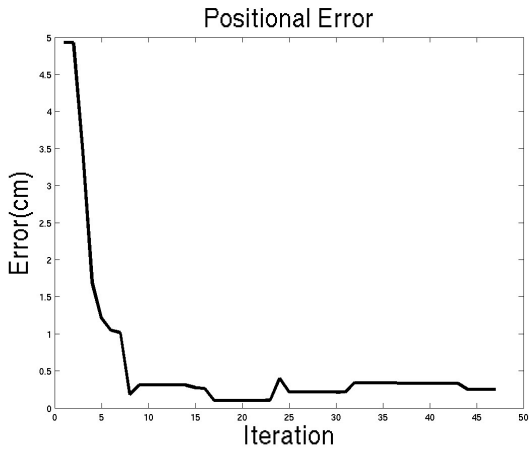


(b) Error in position as a function of iteration

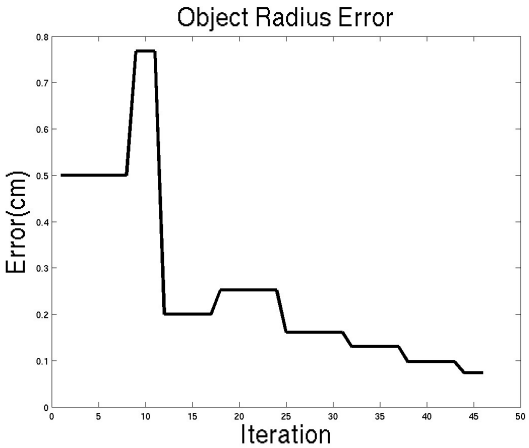


(c) Error in estimated radius as a function of iteration

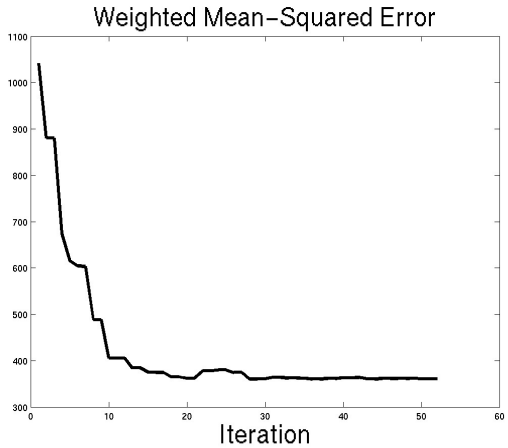


(d) Value of cost function as a function of iteration

Figure 8: